

# Plasmonic Metasurfaces for Coloration of Plastic Consumer Products

Jeppe S. Clausen,<sup>†</sup> Emil Højlund-Nielsen,<sup>‡</sup> Alexander B. Christiansen,<sup>‡</sup> Sadegh Yazdi,<sup>§</sup> Meir Grajower,<sup>||</sup> Hesham Taha,<sup>⊥</sup> Uriel Levy,<sup>||</sup> Anders Kristensen,<sup>\*,‡</sup> and N. Asger Mortensen<sup>\*,†</sup>

<sup>†</sup>Department of Photonics Engineering, <sup>‡</sup>Department of Micro and Nanotechnology, and <sup>§</sup>Center for Electron Nanoscopy, Technical University of Denmark, DK-2800 Kongens Lyngby, Denmark

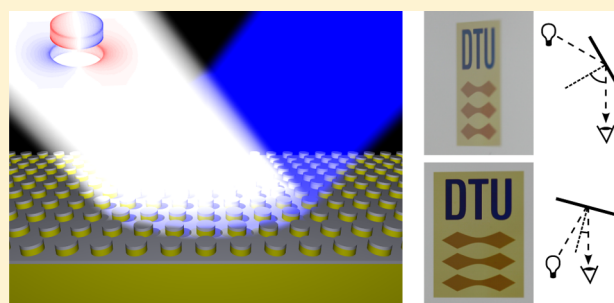
<sup>||</sup>Department of Applied Physics, The Benin School of Engineering and Computer Science, The Center for Nanoscience and Nanotechnology, The Hebrew University of Jerusalem, Jerusalem 91904, Israel

<sup>⊥</sup>Nanonics Imaging Ltd., Hartum 19, Har Hotzvim, Jerusalem 97775, Israel

**S** Supporting Information

**ABSTRACT:** We present reflective plasmonic colors based on the concept of localized surface plasmon resonances (LSPR) for plastic consumer products. In particular, we bridge the widely existing technological gap between clean-room fabricated plasmonic metasurfaces and the practical call for large-area structurally colored plastic surfaces robust to daily life handling. We utilize the hybridization between LSPR modes in aluminum nanodisks and nanoholes to design and fabricate bright angle-insensitive colors that may be tuned across the entire visible spectrum.

**KEYWORDS:** Plasmonics, structural color, hybridization, nanofabrication



Pigment-based coloring of polymers is used in the fabrication of almost any type of plastic-based consumer product, either as base color in the bulk polymer or in surface-decoration inks. The mixing of many colorants in a single product is both costly and limits the possibilities for recycling as separation of the different colorants is impossible. Structural colors offer an attractive approach to reduce the number of needed materials in a given product and it provides new perspectives for recycling and sustainability.

Various strategies may be taken toward structural colors. Inspired by nature<sup>1,2</sup> pure dielectric structures based on photonic crystals in one or more dimensions have been demonstrated<sup>3,4</sup> and recently the use of ultrathin high-loss dielectrics on top of metal have led to bright colors.<sup>5</sup> The works on plasmonic colors have widely emphasized filters working in transmission<sup>6–9</sup> while only more recently plasmonic cavity resonances and LSPR concepts have been used for filters working in reflection.<sup>10–15</sup> The resonant behavior of the plasmonic systems often leads to large field enhancements that are advantageous in other applications such as surface-enhanced Raman spectroscopy.<sup>16–20</sup>

The structural color effects must possess at least three important properties to become relevant for use in consumer products. First, the color effect should be insensitive to varying viewing angles. Furthermore, it should be robust for everyday use. Finally, it should be up-scalable and economically affordable. We demonstrate a plasmonic metasurface that possesses all these qualities. Recently plasmonic resonators consisting of silver and gold have been used for color printing with resolution beyond the diffraction limit.<sup>10,15</sup> We use insight

from hybridization theory<sup>21</sup> to build upon the work of Kumar<sup>10</sup> toward coloration of volume-produced plastic components, addressing the three criteria mentioned above: angle independence, wear resistance, and up-scalability.

Thin metal nanodisks can be tuned in size to modulate the optical response through the visible and near-infrared spectral range.<sup>22</sup> In our work, the colors are based on metal disks on top of dielectric pillars and hovering above a holey metal film, see Figure 1a–c. Rather than employing the common choice of silver or gold, we explore aluminum, which is a widely employed material in industrial processes while so far mainly being conceptually studied as a new plasmonic material.<sup>23–27</sup> Silver and gold are commonly preferred over aluminum for plasmonic applications due to lower ohmic losses. However, we find an advantage of the specific interband absorption properties of aluminum, which gives a pronounced difference in the dispersion of the surface plasmon polaritons (SPPs) supported by the metal–dielectric interfaces of the continuous (holey) film. As demonstrated later, the excitation of SPPs constitutes the main limitation on the angle independence of the observed color and here SPPs supported by aluminum have an advantage over SPPs on silver surfaces due to their k-space existence closer to the “light line” in the frequency range of the visible spectrum. In addition to this, gold has the disadvantage of having an interband transition threshold centered in the

**Received:** April 23, 2014

**Revised:** June 23, 2014

**Published:** July 8, 2014

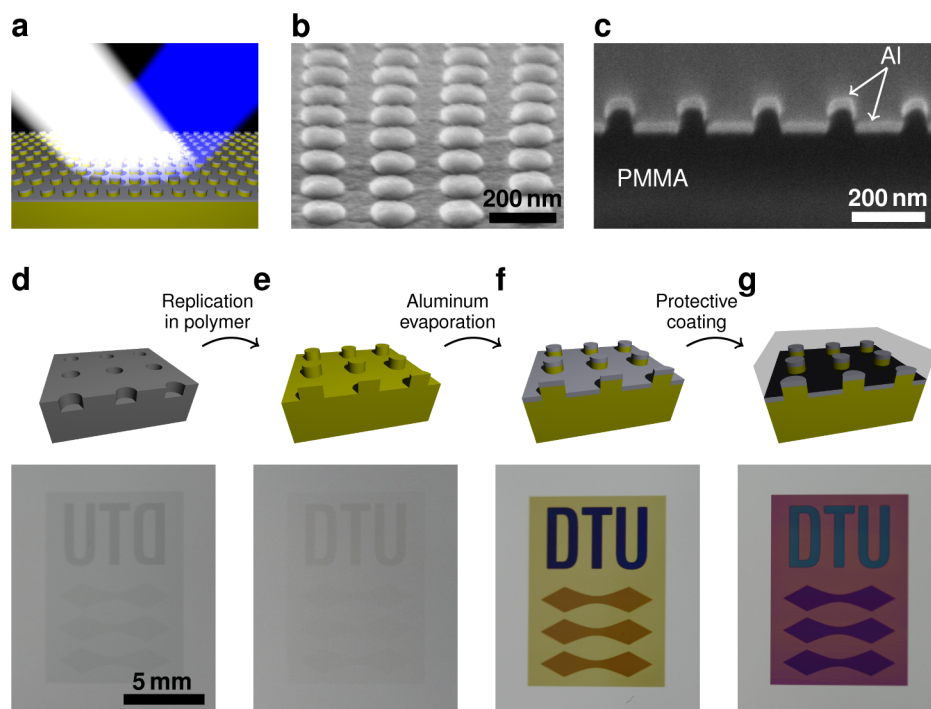


**Figure 1.** Basic concept of fabrication and working mechanism. (a) The reflected light is modified due to absorption resonances in the plasmonic nanostructure leading to colored reflections upon white-light illumination. The reflected color can be varied by tuning the surface geometry. (b) A SEM image of fabricated disks elevated above the holey plane seen from 15° above the horizon. (c) Cross-sectional SEM image obtained using focused ion-beam for sample preparation. (d) A master mold comprising nanohole arrays is used for the fabrication of polymer pillar arrays using hot embossing or injection molding. The photography shows a macroscopic sample with three different hole sizes leading to three different colors in the final sample. (e) A polymer pillar array replication of the master mold. (f) Aluminum is evaporated on top, creating the disk-hole structure thereby revealing colors due to the underlying polymer topography. (g) The structure is coated with a transparent material to protect from greasy contamination, fingerprints, and scratches. The resonance redshift introduced by the coating leads to clearly altered colors.

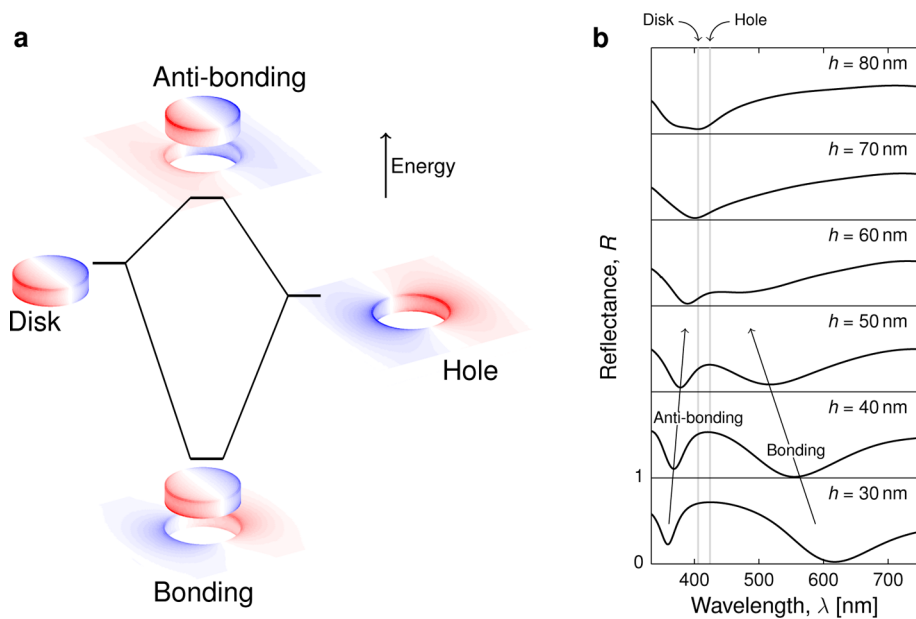


**Figure 2.** Plasmon hybridization due to disk-hole coupling. (a) Energy diagram illustrating the hybridization of the coupled plasmonic modes of the disks and holes of the structure into a low energy mode (bonding) and a high energy mode (antibonding). The simulated charge distributions of the pure disk and hole arrays show the dipolar nature of their resonances. For the full structure, the symmetric and antisymmetric coupling leads to an energy splitting. The shown structure is for  $D = 80$  nm,  $\Lambda = 200$  nm,  $h = 50$  nm, and  $t = 20$  nm embedded in material of refractive index of 1.5. It shows the symmetric and antisymmetric coupling between the disks and holes. (b) Reflectance spectra for same parameters as panel (a) but for varying pillar height,  $h$ . The two modes are seen as dips in the spectra. The coupling and thereby the energy splitting decreases with increasing pillar height leading to a shift of the resonances toward the natural resonances of the disk and hole arrays.

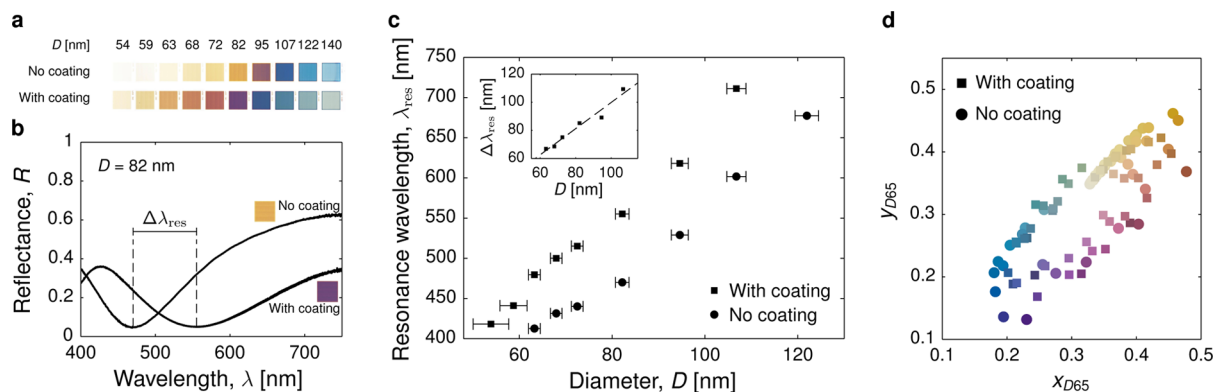


**Figure 3.** Diameter-dependent resonance and colors. (a) Images in bright-field microscopes of  $0.8 \times 0.8 \text{ mm}^2$  squares with period  $\Lambda = 200 \text{ nm}$  and varying diameter. The coating-induced redshift is evident. (b) Reflectance spectra of structure with  $D = 82 \pm 2 \text{ nm}$  with and without coating indicating the change in resonance wavelength  $\Delta\lambda_{\text{res}}$  due to the coating. (c) Resonance position as a function of disk diameter for  $\Lambda = 200 \text{ nm}$ . The shift in resonance due to the coating is seen to be approximately linear with diameter. (d) CIE 1931 chromaticity coordinates of the fabricated samples for both the coated and the uncoated case (spectra in Supporting Information Figure S2). The color of each spot indicates the color of the corresponding sample.

visible spectrum whereas aluminum only facilitates interband transitions in a narrow wavelength range outside the visible spectrum.<sup>28</sup> For large-volume use of plasmonic metasurfaces in, for example, plastic consumables, the abundance and cost of aluminum makes it attractive. The integration in mass-fabrication systems is also eased significantly compared to, for example, silver where the need for an adhesion layer (such as titanium or chromium) and a capping layer (such as gold) to protect against sulphidation, complicates the metal deposition.

The fabrication scheme is presented in Figure 1d–g. A master mold is fabricated in silicon using electron-beam lithography (EBL) and dry etching. A fast single spot writing technique was employed,<sup>29,30</sup> which allows writing speeds higher than  $1 \text{ cm}^2/\text{hour}$  in the production of the silicon masters. This leads to a wider size distribution of the nanostructures than for conventional EBL resulting in inhomogeneous broadening of the resonances. This is however acceptable and compensated by the very large decrease in writing time. The finalized master consists of periodic hole arrays with period  $\Lambda$ , hole diameter  $D$ , and hole depth  $h$ . The master is a negative of the desired polymer surface, a periodic pillar array, which is fabricated in a hot embossing step. After replication, the desired pattern is practically invisible as the polymer–air index contrast is too low to significantly alter the surface reflectance of the nanostructured polymer surface. However, bright and angle-independent colors emerge when a thin aluminum film of thickness  $t$  is deposited on top of the textured polymer surface, see Figure 1f. The metal deposition must be directional in order to facilitate the creation of isolated metal disks. For situations with very large sample size and small evaporation source, this may lead to undesired side-wall deposition thereby defining the maximum sample size. When using roll-to-roll systems, this issue may be avoided due to the continuous deposition of metal.

Finally, a protective coating is deposited on top with a thickness significantly larger than the coherence length of broadband white light in order to avoid Fabry–Pérot interference affecting the color experience. The coating causes an increase in the effective refractive index surrounding the disk-hole nanostructure, which leads to a redshift of the resonances in the system and a corresponding color change as seen in the last step of Figure 1. The top coating is necessary to

protect the structure from mechanical damage, fingerprints, greasy residue, and so forth. In this work, a UV-curable organic–inorganic hybrid material (Ormocomp, Micro resist technology GmbH) with good scratch resistance<sup>31</sup> has been used, but many different types of coatings are already used in large scale production to protect evaporated metal films of various kinds.

The colors of the structure are due to resonant absorption in the aluminum nanostructures. Both the disks and holes possess dipolar resonances on their own, which leads to increased absorption at specific wavelengths. When brought very close together the two modes hybridize into two new modes, a “bonding” mode that is characterized by a lower resonance frequency (longer wavelength) and an “antibonding” mode with higher resonance frequency.<sup>21</sup> Simulated surface charge distributions of the relevant modes are shown in Figure 2a for the specific structure of period  $\Lambda = 200 \text{ nm}$ , diameter  $D = 80 \text{ nm}$ , aluminum thickness  $t = 20 \text{ nm}$ , and pillar height  $h = 50 \text{ nm}$ . The low-energy mode is characterized by the charge oscillations in the disk and the hole being out-of-phase whereas for the high energy mode the charge oscillations are in phase. The effect on the reflectance spectrum is illustrated in Figure 2b where each of the two hybrid modes appear as significant dips in the reflectance spectra. It is seen how the energy splitting decreases, when the pillar height,  $h$ , increases thereby decreasing the coupling between the resonators. It is also seen that the strength of the “bonding” mode is highly dependent on low pillars (large coupling) and above  $h = 70 \text{ nm}$  the hybridization is not seen in the reflectance spectra. For even higher pillars,<sup>32</sup> the behavior of the system moves toward a Fabry–Pérot-like regime where the disk array and the hole array each acts as separate mirrors with resonant reflection coefficients. It is found that when using aluminum as the plasmonic material a strong resonance of the hybrid “bonding” mode is key to the creation of tunable colors. This is seen from simulations (Supporting Information, Figure S1), which demonstrate how it is possible with strong coupling (low pillars) to obtain resonances across the entire visible spectrum by tuning the pillar diameter, while for vague coupling (high pillars) no such tuning is possible. Because we mainly utilize the “bonding” mode resonance we will in the following just denote the wavelength of this resonance  $\lambda_{\text{res}}$ .

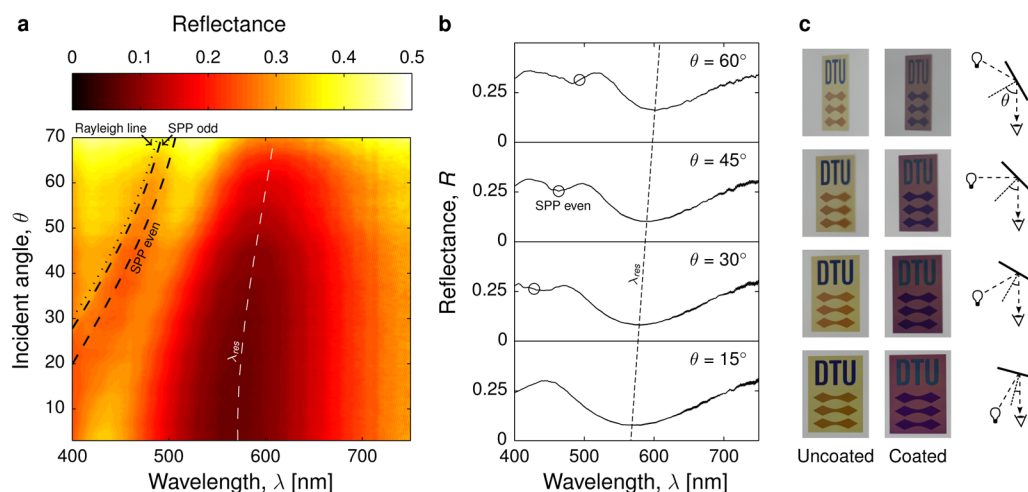


**Figure 4.** Angle dependence of reflected spectrum. (a) Measured angle-resolved spectra of coated sample with  $\Lambda = 200$  nm and  $D = 86 \pm 2$  nm. The white dashed line indicates the reflectance minimum and the black dashed lines indicate the theoretical excitation of SPPs (odd and even modes) in a 20 nm Al film embedded in material of refractive index 1.5. The dotted line indicates the appearance of new diffraction orders (Rayleigh wavelength). The resonance is seen to shift very little even at very high angles. (b) Single spectra at four different angles of the same sample as in panel a. (c) Pictures of macroscopic patterns viewed at four different angles. The colors are seen to be almost identical even for very large angles. The gray background is the unstructured surface of the samples.

While securing the existence of the important hybrid “bonding” mode by fabricating very low pillars one must keep in mind that it is of great importance that the disks are separated from the lower lying film to avoid short circuiting of the capacitively coupled disk and hole planes. By preparing a cross section sample, using focused ion beam (FIB), we can confirm that in majority of cases the disk and the lower lying film are separated, see Figure 1c.

In the fabrication of the polymer pillars a certain rounding at the pillar end-face should be expected, compared to the perfect cylindrical shape used in simulations. The rounding is seen in Figure 1c. This effectively reduces the vertical gap between the disk and hole, which is why it is necessary to fabricate the pillars slightly higher than predicted by simulations for achieving comparable coupling. Fabricated pillars were  $h = 56 \pm 4$  nm high, measured by atomic force microscope, and the aluminum thickness was  $t = 20$  nm, measured by quartz crystal microbalance during deposition.

The fixed pillar height and metal thickness leave the diameter and period as design parameters. In this work, diameters between 40–160 nm and periods ranging from 160 to 240 nm have been studied experimentally. Figure 3a shows color photos of  $\Lambda = 200$  nm samples with and without the presence of a protective coating. Colors across the entire visible spectrum are produced at will by varying the disk diameter at fixed period. The measured reflectance spectra of disks with diameter  $82 \pm 2$  nm are shown as example in Figure 3b. The coating induces a redshift  $\Delta\lambda_{\text{res}}$  of the resonance due to increase in effective refractive index around the nanostructure. One should notice the high off-resonant reflectance in contrast to the low reflectance at resonance, which leads to very bright colors. For both the coated and uncoated case, the resonance position increases almost linearly with diameter. Specifically for the coated case, the resonance may be tuned on the wavelength interval 400–700 nm by tuning the diameter on the interval 50–110 nm. The coating-induced redshift is also found to increase linearly with diameter. Reflectance spectra for the other periods and diameters are provided in the Supporting Information (Figure S2). The effect of the period on the

resonance position is less pronounced as it only influences the mutual coupling of neighboring resonators. The nearest-neighbor coupling does however influence how much a change in diameter alters the resonance position (the slope of Figure 3c). For a coated sample with  $\Lambda = 160$  nm, a 1 nm increase in diameter leads to an approximate redshift of 7 nm whereas for  $\Lambda = 240$  nm it only leads to an approximate redshift of 4 nm (see Supporting Information Figure S3). Although the period does not influence the resonance position significantly, it plays an important role in relation to the angular dependence.

The range of colors that may be produced using the proposed method is illustrated in Figure 3d where all experimentally measured spectra (see Supporting Information Figure S2) have been converted to CIE1931 chromaticity coordinates, thereby illustrating the color gamut of the method. It is noteworthy that there are points all around the achromatic point, illustrating the large degree of color tuning ability. There are however some colors that are difficult to produce when the effect is based on a spectral dip originating from resonant absorption. Very chromatic red and green are examples of such colors.

The angle independence of the reflective colors was investigated on larger samples ( $4 \times 6$  mm<sup>2</sup>). The specular reflectance was measured with unpolarized light for incident angles at 3–70°, see Figure 4. Data are shown for a coated sample with  $\Lambda = 200$  nm and  $D = 86 \pm 2$  nm. In the surface plot of Figure 4a, the broad dip in the reflectance is observed around a vacuum wavelength of 580 nm and is slightly red shifted by approximately 20 nm for increasing angle of incidence. This is the diameter-dependent plasmonic absorption resonance described previously. Individual reflectance spectra for four different angles are shown in Figure 4b, and the photographs in Figure 4c illustrate the angle independence of the color appearance. The changes of the CIE1931 chromaticity coordinates due to changing angles have been calculated based on the angle-resolved spectra and are presented in the Supporting Information (Figure S4). As seen in panels a and b, the strength of the resonance dip decreases with increasing angle of incidence. This is due to a decreasing component of

the electric field of the TM mode parallel to the dipole axis under consideration. A weak angle-dependent feature is observed at vacuum wavelength below 500 nm, which is caused by grating-assisted excitation of SPPs at the metal–dielectric interfaces. The dashed black lines indicate the calculated dispersion of the odd and even modes for a 20 nm aluminum film embedded in a material of refractive index 1.5. The Rayleigh line, where the first diffraction order appears, is plotted as a dotted line. Of the three anomalies, the even (high loss) SPP mode lies in the center of the angle-dependent dip, and in Figure 4b the circles indicate the position of this mode. It corresponds well with the dips in the measured reflectance spectra and the feature is attributed to this mode. The positions of the SPP anomalies depend on the grating-induced change in momentum parallel to the surface and are therefore highly dependent on the structure period. A longer grating period,  $\Lambda$ , will result in the anomalies appearing at lower angles, implying a higher degree of angle dependence, whereas a shorter period will lead to less impact on the spectra (see Figure S5 in Supporting Information). This implies a trade-off between obtaining low angular dependence and fabrication limitations due to dense structures with small grating period. Properties of the SPP modes have been investigated using near-field scanning optical microscopy (NSOM). The data are presented in the Supporting Information (Figure S6).

While the position of the Rayleigh line only depends on the grating period and the refractive index of the materials surrounding the metal, the dispersion relation for the SPPs also has a strong dependence on the dielectric constant of the metal. Hence, the position of the angle-dependent SPP modes (relative to the localized mode) makes the feasibility of angle-independent plasmonic structural colors strongly material dependent. As an example, we compare aluminum and silver in the Supporting Information (Figure S5). For aluminum, the SPP modes lie very close to the Rayleigh line and may therefore be moved out of the visible spectrum, even for high incident angles by using small periods. On the other hand, for silver films SPPs are excited at normal incidence, even for very short periods whereby the SPP modes spectrally intersect with the localized modes. This leads to phenomena such as avoided crossing between the two intersecting modes resulting in significant angle-dependent behavior of the color-producing mode. Because this is a property originating from the electronic structure of the chosen metal, this promotes aluminum over silver for use in this application.

Because of the subwavelength periodic nature of the structure, the color effect is only seen in the specular reflection. This limits the applicability under certain lighting conditions. For diffuse lighting conditions, an observer will experience uniform color, while illumination by very directional light sources will lead to a more varying color experience. To overcome this problem, one may introduce scattering in the protective film either by particles, surface roughness or by using semicrystalline (translucent) polymers as coating material. This will allow for diffuse reflectance from the surface similar to that of inks.

In conclusion, we demonstrate angle-insensitive scratch-resistant structural colors, where aluminum is used as a cheap and abundant plasmonic material. We utilize a hybrid disk-hole plasmonic mode, which provides angle-independent resonances tunable across the entire visible spectrum. Expensive nanolithography should only be carried out once due to the subsequent replication-based fabrication and the structure

geometry allows for a fast EBL technique to define macroscopic wafer-sized patterns. The functional structures are covered by a protective dielectric coating, causing a redshift of the plasmon resonance. The method holds potential for large scale implementation of structural colors in plastic products for daily use.

## ■ ASSOCIATED CONTENT

### 📄 Supporting Information

Details about fabrication process, optical characterization, and simulations as well as supplementary figures (Figures S1–S6). This material is available free of charge via the Internet at <http://pubs.acs.org>.

## ■ AUTHOR INFORMATION

### Corresponding Authors

\*E-mail: (A.K.) [anders.kristensen@nanotech.dtu.dk](mailto:anders.kristensen@nanotech.dtu.dk)

\*E-mail: (N.A.M.) [asger@mailaps.org](mailto:asger@mailaps.org)

### Notes

The authors declare no competing financial interest.

## ■ ACKNOWLEDGMENTS

The authors thank Cameron Smith and Christoph Vannahme for advice on microscope measurements and Thomas Christensen for fruitful discussions on the data interpretation. The work was supported by the Danish National Advanced Technology Foundation (Contract No.: 007-2010-2) via the NanoPlast project and by the European Commission via the FP7MMP Integrated project PLAST4FUTURE (NMP2-SE-2012-314345). The work was also supported by the Danish Agency for Science, Technology and Innovation (International Network Programme, Israel-Danish international collaboration, Framework Grant 1370-00124A).

## ■ REFERENCES

- (1) Vukusic, P.; Sambles, J. R. *Nature* **2003**, *424*, 852–855.
- (2) Kinoshita, S.; Yoshioka, S.; Miyazaki, J. *Rep. Prog. Phys.* **2008**, *71*, 076401.
- (3) Saito, A.; Miyamura, Y.; Nakajima, M.; Ishikawa, Y.; Sogo, K.; Kuwahara, Y.; Hirai, Y. *J. Vac. Sci. Technol. B* **2006**, *24*, 3248–3251.
- (4) Chung, K.; Yu, S.; Heo, C.-J.; Shim, J. W.; Yang, S.-M.; Han, M. G.; Lee, H.-S.; Jin, Y.; Lee, S. Y.; Park, N.; Shin, J. H. *Adv. Mater.* **2012**, *24*, 2375–2379.
- (5) Kats, M. A.; Blanchard, R.; Genevet, P.; Capasso, F. *Nat. Mater.* **2013**, *12*, 20–24.
- (6) Ebbesen, T. W.; Lezec, H. J.; Ghaemi, H. F.; Thio, T.; Wolff, P. A. *Nature* **1998**, *391*, 667–669.
- (7) Lee, H.-S.; Yoon, Y.-T.; Shin Lee, S.; Kim, S.-H.; Lee, K.-D. *Opt. Express* **2007**, *15*, 15457–15463.
- (8) Xu, T.; Wu, Y.-K.; Luo, X.; Guo, L. J. *Nat. Commun.* **2010**, *1*, 59.
- (9) Inoue, D.; Miura, A.; Nomura, T.; Fujikawa, H.; Sato, K.; Ikeda, N.; Tsuya, D.; Sugimoto, Y.; Koide, Y. *Appl. Phys. Lett.* **2011**, *98*, 093113.
- (10) Kumar, K.; Duan, H.; Hegde, R. S.; Koh, S. C. W.; Wei, J. N.; Yang, J. K. W. *Nat. Nanotechnol.* **2012**, *7*, 557–561.
- (11) Lochbihler, H. *Opt. Lett.* **2013**, *38*, 1398–1400.
- (12) Wu, Y.-K. R.; Hollowell, A. E.; Zhang, C.; Guo, L. J. *Sci. Rep.* **2013**, *3*, 1194.
- (13) Si, G.; Zhao, Y.; Lv, J.; Lu, M.; Wang, F.; Liu, H.; Xiang, N.; Huang, T. J.; Danner, A. J.; Teng, J.; Liu, Y. J. *Nanoscale* **2013**, *5*, 6243–6248.
- (14) Yan, M.; Dai, J.; Qiu, M. J. *Opt.* **2014**, *16*, 025002.
- (15) Roberts, A. S.; Pors, A.; Albrektsen, O.; Bozhevolnyi, S. I. *Nano Lett.* **2014**, *14*, 783–787.

- (16) Chu, Y.; Banaee, M. G.; Crozier, K. B. *ACS Nano* **2010**, *4*, 2804–2810.
- (17) Caldwell, J. D.; Glembocki, O.; Bezares, F. J.; Bassim, N. D.; Rendell, R. W.; Feygelson, M.; Ukaegbu, M.; Kasica, R.; Shirey, L.; Hosten, C.; Al, C. E. T. *ACS Nano* **2011**, *5*, 4046–4055.
- (18) Li, W.; Hu, J.; Chou, S. *Opt. Express* **2011**, *19*, 21098–21108.
- (19) Li, W.; Ding, F.; Hu, J.; Chou, S. *Opt. Express* **2011**, *19*, 863–870.
- (20) Cheng, C.-W.; Abbas, M. N.; Chiu, C.-W.; Lai, K.-T.; Shih, M.-H.; Chang, Y.-C. *Opt. Express* **2012**, *20*, 10376–10381.
- (21) Prodan, E.; Radloff, C.; Halas, N.; Nordlander, P. *Science* **2003**, *302*, 419–422.
- (22) Manjavacas, A.; García de Abajo, F. J. *Nat. Commun.* **2014**, *5*, 3548.
- (23) Chen, Q.; Cumming, D. R. S. *Opt. Express* **2010**, *18*, 14056–14062.
- (24) Langhammer, C.; Schwind, M.; Kasemo, B.; Zorić, I. *Nano Lett.* **2008**, *8*, 1461–1471.
- (25) Chan, G. H.; Zhao, J.; Schatz, G. C.; Van Duyne, R. P. *J. Phys. Chem. C* **2008**, *112*, 13958–13963.
- (26) Knight, M. W.; Liu, L.; Wang, Y.; Brown, L.; Mukherjee, S.; King, N. S.; Everitt, H. O.; Nordlander, P.; Halas, N. J. *Nano Lett.* **2012**, *12*, 6000–6004.
- (27) Knight, M. W.; King, N. S.; Liu, L.; Everitt, H. O.; Nordlander, P.; Halas, N. J. *ACS Nano* **2014**, *8*, 834–840.
- (28) Zorić, I.; Zäch, M.; Kasemo, B.; Langhammer, C. *ACS Nano* **2011**, *5*, 2535–2546.
- (29) Gadegaard, N.; Thoms, S.; Macintyre, D. S.; Mcghee, K.; Gallagher, J.; Casey, B.; Wilkinson, C. D. W. *Microelectron. Eng.* **2003**, *68*, 162–168.
- (30) Højlund-Nielsen, E.; Greibe, T.; Mortensen, N. A.; Kristensen, A. *Microelectron. Eng.* **2014**, *121*, 104–107.
- (31) Sanchez, C.; Julin, B.; Belleville, P.; Popall, M. J. *Mater. Chem.* **2005**, *15*, 3559–3592.
- (32) Lochbihler, H.; Ye, Y. *Opt. Lett.* **2013**, *38*, 1028–30.